ACS OMEGA

Open Access

http://pubs.acs.org/journal/acsodf

Article

CuAAC "Click"-Derived Luminescent 2-(2-(4-(4-(Pyridin-2-yl)-1*H*-1,2,3-triazol-1-yl)butoxy)phenyl)benzo[*d*]thiazole-Based Ru(II)/Ir(III)/Re(I) Complexes as Anticancer Agents

Lavanya Thilak Babu and Priyankar Paira*

Cite This: *ACS Omega* 2023, 8, 32382−32395

Read Online

ACCESS | Metrics & More | Article Recommendations | Supporting Information

ABSTRACT: To enhance the cytoselective behavior of the complexes, we intended to develop a CuAAC "click"-derived synthetic protocol for the preparation of 2-(2-(4-(4-(pyridin-2-yl)-1*H*-1,2,3-triazol-1-yl)-butoxy)phenyl)benzo[*d*]thiazole-based Ru(II)/Ir(III)/Re(I) complexes, and their cytotoxicity against three different cancer cell lines (MCF-7, HeLa, and U87MG) in consort with one normal cell line (HEK-293) was evaluated. In our detailed investigations, the significant cytotoxic nature of the Ru(II) complex **7a** compared to Ir(III) and Re(I) complexes (**7b** and **7c**, respectively) was observed. Complex **7a** was capable of MCF-7 cell apoptosis via the inhibition of both S- and G2/M-phase cell cycle arrest in association with a substantial quantity of ROS production and DNA intercalation.

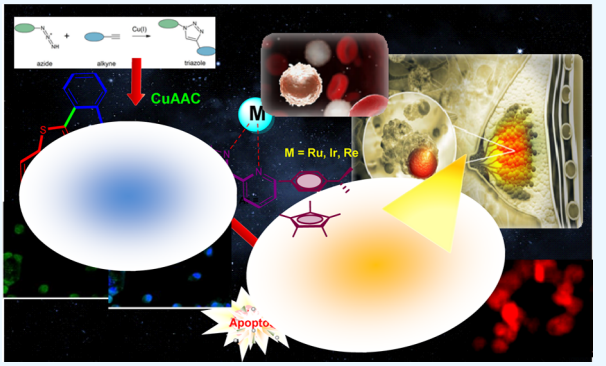

1. INTRODUCTION

The intricate nature of cancer makes it a terminal and leading cause of death worldwide.[1] The global cancer cases are predicted to show an upsurge by 28.4 million in 2040.[2] Researchers have been inquisitive in the forage for newfangled anticancer drugs, yet it remained muddled until the advent of *cis*-diamminedichloroplatinum(II). This laid the foundation for an era of neoplastic drugs based on metal-based complexes. Since then, scientists have endeavored to study organometallic transition metals as antitumor drug candidates.[3] Traditionally, metal-based compounds date back to the ancient period due to their therapeutic value. Earlier, the primary concern regarding metal-based compounds was the lack of a clear understanding of the therapy and dose−response knowledge.[4] Nowadays, advanced, up-to-date tools and a better understanding of cancer mechanisms have led to the development of multifunctional anticancer drugs with higher selectivity toward tumors.[5,6] A significant limitation of cisplatin includes inherent and acquired resistance, concomitant side effects, and reduced tumor treatment.[7] These shortcomings made scientists think of alternative metallodrugs that can overcome the drawbacks faced by cisplatin.[8] An accurate cancer diagnosis is imperative for felicitous and effective cancer treatment because each cancer type requires a specified regimen.[9] Metallic complexes show excellent kinetic stability and are reactive due to metal−carbon bonds and π-bound arene.[10] Moreover, the transition metal arene system regulates its hydrophilicity and hydrophobicity, leading to more productive uptake in cancer cells than normal cells. In addition, the presence of labile chlorine in metallodrugs makes them more reactive toward nucleobases.[11]

Extensive research is ongoing on metal-based drugs with higher cytotoxicity and selectivity toward neoplastic cells, low resistance, and fewer side effects.[11] Currently, a number of cost-effective and cytoselective ruthenium complexes have been developed for their high aqueous and glutathione (GSH) stability, high water solubility, sluggish ligand-exchange kinetics, and various oxidation states (II, III, and IV) under different physiologically relevant conditions.[12−14] Furthermore, the higher selectivity of these complexes against cancer cells compared to normal cells make them potential anticancer agents against some cisplatin-resistant cell lines.[15] Besides KP1339, many other Ru(II)−arene complexes comprising AH54 and AH63 established for human colorectal cancer cells and certainly phototoxic TLD1433 are in clinical trial.[16−20] Iridium (III) complexes have also been established as potential anticancer agents because of their adaptable photophysical properties, besides fewer side effects.[21] Likewise, the mechanism of action (MoA) of Ir(III)−Cp* complexes in cancer cells was evaluated by Sadler group.[22] Lu et al. revealed the anti-metastasis and anti-breast cancer tumorigenesis activity of sulfur-coordinated organoiridium (III) complexes containing C, N- and S, S-chelating ligands by targeting the

Received: March 10, 2023
Accepted: July 13, 2023
Published: August 30, 2023

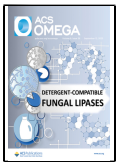

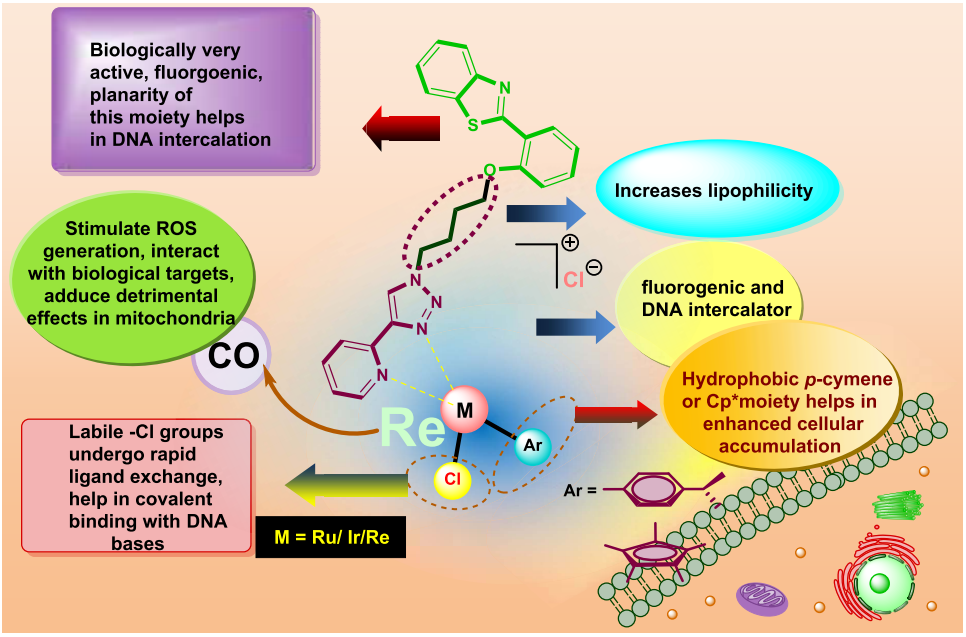

Figure 1. Design of the luminescent anticancer 2-(2-(4-(4-(pyridin-2-yl)-1*H*-1,2,3-triazol-1-yl)butoxy)phenyl)benzo[*d*]thiazole-based Ru(II)/Ir(III)/Re(I) complexes.

Scheme 1. Synthetic Route for the CuAAC "Click"-Derived 2-(2-(4-(4-(Pyridin-2-yl)-1*H*-1,2,3-triazol-1-yl)butoxy)phenyl)benzo[*d*]thiazole (6)

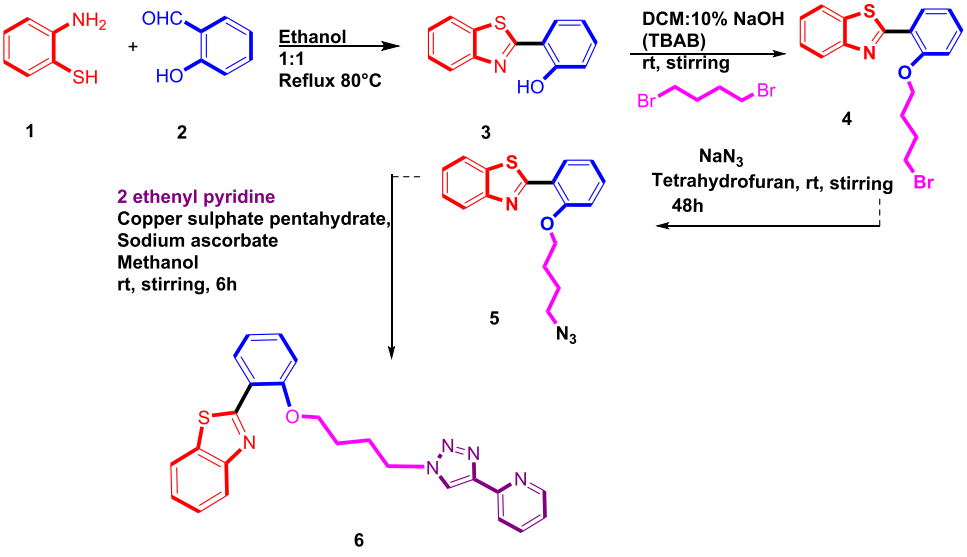

Wnt/β−catenin signaling pathway, where the complexes activated the dereliction of LRP6 shrinking the protein levels of DVL2 (β-catenin and activated β-catenin) along with the downregulation of Wnt target genes—CD44 and survivin.[23] The cellular redox balance is also disturbed by Ir(III) complexes, which in turn causes lipid peroxidation as well as ferroptosis in cancer cells and activates immunogenic cell death (ICD).[24] Instead, rhenium(I) tricarbonyl complexes exhibit extraordinary properties such as high photostability, polarized emission, a large Stokes shift, and prolonged lifetimes, which are applicable for bioimaging as well as cancer therapy.[25,26] Not only that, Re(I) displays a d^6 electronic configuration in its outermost shell and thus possesses high biocompatibility. Re(I) tricarbonyl complexes also exhibited the same order of ligand-exchange kinetics as platinum-based drugs; nevertheless, these complexes are superior to anticancer platinum complexes for their unresolved spectroscopic properties, i.e., triplet-state luminescent emission laterally with their discrete C≡O stretching frequency.[27] Considering the distinction of Ru(II), Re(I), and Ir(III) metals, the incorporation of bioactive ligands has expanded significantly because of their multitargeting properties, which can enhance the anticancer properties of metal complexes. Many benzothiazole derivatives have shown potency in various cancer cell lines by different mechanisms of action, some of which are poorly explored.[28]

Hence, considering all of the advantages of ruthenium, rhenium, and iridium metals as well as the benzothiazole moiety in focus, the current work targets to improve well-characterized luminescent 2-(2-(4-(4-(pyridin-2-yl)-1*H*-1,2,3-triazol-1-yl)butoxy)phenyl)benzo[*d*]thiazole-based Ru(II)/Re-

https://doi.org/10.1021/acsomega.3c01639
ACS Omega 2023, 8, 32382−32395

Scheme 2. Synthetic Route for Ru(II)/Ir(III)/Re(I)-Based N∧N Complexes (7a−c)

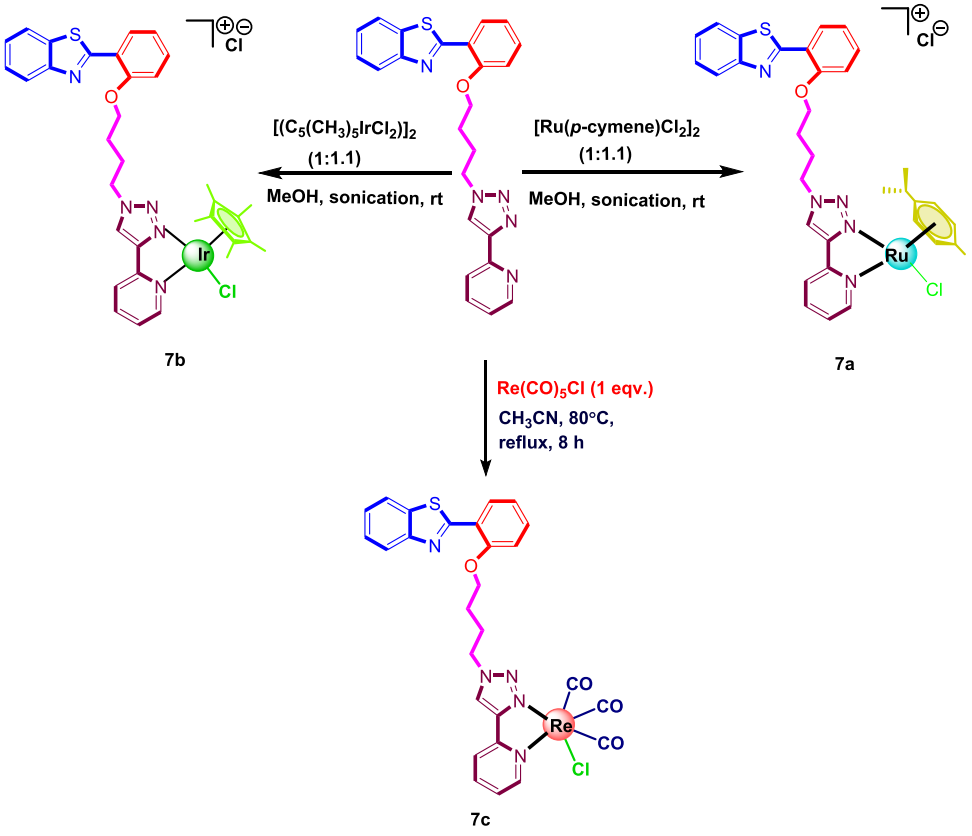

(I)/Ir(III) complexes for selective cancer therapy (Figure 1). There are several features in the synthesized molecules that facilitate the inhibition of cell proliferation, including the following: (i) the addition of an alkyl spacer linker in the ligand enhances its lipophilicity; (ii) the (pyridin-2-yl)-1*H*-1,2,3-triazole scaffold enhances the fluorogenic behavior of the molecule and also acts as DNA intercalator; (iii) hydrophobic *p*-cymene and cp* improve the lipophilic properties of the molecule and enhance cellular accumulation; (iv) labile chlorine undergoes rapid ligand exchange and helps in biomolecular interaction; (v) the −CO group present in the rhenium complexes stimulates ROS generation and interacts with the biological target.

2. RESULTS AND DISCUSSION

2.1. Chemistry. *2.1.1. Synthesis and Characterization.* Initially, we synthesized 2-hydroxyphenyl benzothiazole (**3**) by condensing 2-amino thiophenol (**1**) and salicylaldehyde (**2**) under reflux conditions. The resultant compound **3** has an -OH group that undergoes an alkylation reaction by adding 1,4 dibromo butane using 10% NaOH as a base under phase-transfer catalytic conditions. After the reaction, column chromatography was performed using a hexane/ethyl acetate (99:1) V/V solvent system, and the desired compound **4** was isolated from the dimers. The formed bromoalkoxy benzothiazole **4** was then further converted to azide by reaction with sodium azide in THF at ambient temperature. Azidoalkoxy benzothiazole **5** was further reacted with 2-ethenyl pyridine *via* a click reaction using a reaction mixture of copper sulfate pentahydrate and sodium ascorbate in a THF/water (8:2 v/v ratio) solvent system under heating at 60 °C to synthesize the desired triazole product (**6**) (Scheme 1).

The synthesized triazole (**6**) was further reacted with [Ru(*p*-cymene)Cl_2]$_2$, a pentamethyl cyclopentadienyl iridium (III) chloride dimer, and pentacarbonylchloro rhenium(I) to form the desired metal complexes (**7a−c**) (Scheme 2). Intermediates **3**, **4**, **5**, the ligand **6**, and the corresponding complexes (**7a−c**) were thoroughly characterized by NMR spectroscopy, FT-IR spectroscopy, and mass spectrometry. In the ^{1}H NMR spectra, the typical singlet -OH peak of compound **3** at a downfield region (δ 12.56 ppm) and aryl CH protons at δ 6.9−8.0 ppm were observed. In compound **4**, the singlet -OH peak was absent, and the presence of -CH_2 peaks in the shielded region (δ 2−4 ppm) confirms its formation. The -CH_2 peaks found near oxygen and bromine were deshielded (δ 4.2 and 3.5 ppm) due to their electronegativity. At the same time, the other two CH_2 groups present in the linker were observed as multiplets at δ 2.2 ppm. The apparent splitting of the four CH_2 groups was observed in compound **5** due to the presence of the electron-withdrawing group N_3; the adjacent proton was deshielded. In the ^{1}H NMR spectra, the characteristic peak of the triazole ring and pyridine ring at δ 6−8 ppm confirms the formation of ligand **6**. The formation of compound **6** was further established by the ESI-MS signal at an *m*/*z* of 428.4 $[M + H]^+$.

The ^{1}H NMR spectra of ligand **6** and its corresponding Ru(II) complex **7a** varied immensely, exhibiting peaks attributed to methyl protons around δ 2.29 ppm and those attributed to isopropyl protons of *p*-cymene at δ 0.86−0.95 ppm. In the ^{1}H NMR spectrum, aromatic peaks of *p*-cymene were found in the δ 5.8−6.2 ppm region. The exact mass of complex **7a** was calculated to be 700.15, and the abundance peak was located in the spectrum at 700.8 $[M]^+$, along with a characteristic ruthenium isotopic splitting pattern. Further-

https://doi.org/10.1021/acsomega.3c01639
ACS Omega 2023, 8, 32382−32395

Table 1. Photophysical Characterization, Conductivity, and Lipophilicity Study of the Complexes (7a−c)

	λ_a (nm)[a]								^M (S cm^2 mol^{-1})[g]	
samples	$\pi-\pi^*$	MLCT	λ_f (nm)[b]	Stokes shift	OD[c]	ε ($M^{-1}cm^{-1}$)[d]	ϕ_f[e]	log $P_{o/w}$[f]	DMSO	10% DMSO
7a	328		382	54	1.07	35 666	0.0193	0.9268	8	30
7b	326	∼400	380	54	0.19	6333	0.0004	0.5652	5	26
7c	337	∼400	377	40	0.37	12 333	0.0140	0.3180	9	22
quinine sulfate	350		452	102	0.26	8000	0.546			

[a]Absorption maxima. [b]Emission wavelength. [c]Optical density. [d]Extinction coefficient. [e]Quantum yield. [f]*n*-Octanol/water partition coefficient. [g]Conductance in DMSO and 10% aqueous DMSO.

more, in complex **7b**, the characteristic peak for 15 Cp* protons is exhibited at δ 1.6 ppm in the ^{1}H NMR spectrum. The mass of complex **7b** was obtained at 791.8 $[M]^+$ in the ESI-MS spectrum, which exactly matched the theoretical value. In complex **7c**, there was no change in the ^{1}H NMR spectrum after complex formation. Therefore, the primary confirmatory assays included ^{13}C NMR technique, FT-IR spectroscopy, and ESI-MS. Complex **7c** formation was confirmed by the ^{13}C NMR spectrum, wherein carbonyl peaks were observed around 190 ppm. In the FT-IR spectrum of complex **7c**, the stretching frequency for C═O was assigned in the regions 1876 and 2019 cm^{-1}. In the ESI-MS spectrum, the characteristic peak at 734.4 $(M + H)^+$ confirms the formation of the Re(I)−HBT complex. In the FT-IR spectra of all complexes, with the alkyl group as a linker, the absorption bands of the (C−H) sp^3 asymmetric stretching were observed around 2958 to 2959 cm^{-1} and those of the symmetric stretchings were observed around 2851 to 2855 cm^{-1}. The absorption peaks at 1627, 1632, and 1594 cm^{-1} were assigned to the C═N stretching peaks in all three synthesized complexes, respectively.

2.2. Physicochemical Studies. *2.2.1. Electronic Absorption (UV−Visible) and Fluorescence Study.* To evaluate the cellular-imaging properties of these complexes (**7a−c**), UV−visible and fluorescence studies were carried out in 0.1% DMSO buffer solution at pH 7.2 (Figure S1). UV−visible spectroscopy revealed that these complexes were able to exhibit robust absorption bands in the range of 300−400 nm attributable to significant intraligand (N∧N) charge transfer (LLCT) transitions and insignificant metal-to-ligand charge transfer (MLCT). In the fluorescence spectra, all of these complexes displayed emissions in the range of 370−600 nm because of LLCT by electronic transitions from a higher energy to a lower energy π-molecular orbital of the ligand on exciting the molecules at around 300 nm. From the emission spectra, the conforming quantum yields (Φ_f) of these complexes were calculated from eq i using quinine sulfate as a relative reference standard. For complexes **7a**, **7b**, and **7c**, the quantum yields were computed as 0.0019, 0.0004, and 0.0140, respectively (Table 1).

2.2.2. Solubility, Conductivity, and Lipophilicity Studies. The balance between hydrophilicity and lipophilicity is an important factor determining the tumor-shrinking ability of metal complexes. Therefore, to evaluate the drug-like characteristics of these complexes, a lipophilicity study was conducted *via* the shake-flask method. It was observed that all of these complexes were highly soluble in DMF and DMSO, and satisfactorily soluble in acetonitrile, methanol, and ethanol. Although the Re(I) complex (**7c**) exhibited poor solubility in water, Ru(II) (**7a**) and Ir(III) complexes (**7b**) showed very good solubility in aqueous medium. The solubilities of these complexes at 25 °C were in the range of 5−8 mg/mL of the DMSO-10% DMEM medium (1:99 v/v, comparable to cell media). In order to provide considerable lipophilicity to these complexes (**7a−c**), we determined the n-octanol/water partition coefficient (log $P_{o/w}$, where $P_{o/w}$ = octanol/water partition coefficient; eq ii) by the conventional shake-flask method (Table 1).[29] The experimental log $P_{o/w}$ values of these complexes were observed to be in the range of 0.31−0.92. The highest and lowest log $P_{o/w}$ values were observed in complexes **7a** and **7c**, respectively. The molar conductance values of all of these complexes were found to be in the range of 5−9 S cm^2 mol^{-1} in pure DMSO solution. Moreover, their conductance increased to 22−30 S cm^2 mol^{-1} in 10% DMSO solution (Table 1). This is due to the change in the electrolytic behavior during the dissociation of the M−Cl bond, causing the formation of aqua complexes in the bulk aqueous medium.

2.3. Biology. *2.3.1. DNA-Binding Studies. 2.3.1.1. UV Absorption Method.* Ct-DNA-binding studies were conducted for metallic complexes (**7a−c**) to understand the nature of binding with DNA in a 5 mM Tris-HCl/50 mM NaCl buffered medium at pH 7.2. The purity of Ct-DNA was determined using a UV−vis spectrophotometer by detecting its OD at 260 and 280 nm wavelengths. The purity was 1.86, within the 1.8−1.9 range, which indicates a pure form, free from proteins. Nucleic acids exhibit significant absorption in the range of 240−275 nm. This is due to the $\pi-\pi^*$ transitions of the base pair pyrimidine and purine nucleobases.[30] The Ct-DNA-binding experiment was carried out by fixing the complex concentration (5×10^{-5} μM) and sequentially increasing the concentration of Ct-DNA (5−60 μM). Spectral changes in the absorbance of all of the complexes (**7a−c**) were studied, and they were found to exhibit a hypochromic shift. The absorbances of these complexes (**7a−c**) at their $\pi-\pi^*$ absorption wavelengths of 320, 331, and 325 nm gradually decreased with an increase in the Ct-DNA concentration, along with an isosbestic point in the 286−289 nm range. Henceforth, these complexes can be considered good DNA intercalators because of the considerable planarity of the ligand (**6**) intercalated into the nucleic acid. During intercalation into DNA, the complexes position themselves in between the nucleobases and stabilize them, which in turn changes the length of the DNA, unwinding them, and therefore, the aromatic rings of bases are exposed to UV light more frequently, and as a result, there is obvious hyperchromism around 260 nm. The intercalating complex (**7a−c**) into DNA is further stabilized by stacking interactions, which led to an overlap in $\pi-\pi^*$ electronic states and a reduction in HUMO and LUMO energy gap levels, supporting a bathochromic shift.[31] The sharp isosbestic points at 287, 286, and 289 nm indicate that these complexes exist in two different states (bound and free forms) and that adduct formation results in the interaction between complexes and DNA. Although intercalation causes a spectral shift leading to hypochromic and bathochromic effects, even in the case of groove binding,

https://doi.org/10.1021/acsomega.3c01639
ACS Omega 2023, 8, 32382−32395

similar changes are observed in the UV−vis spectrum. These findings suggested that intercalation, together with groove binding, may be the preferred binding mode for all of these synthesized complexes.[31,32] The intrinsic binding constant (K_b) values for complexes **7a**, **7b**, and **7c** were evaluated from the linear [DNA]/($\varepsilon_a - \varepsilon_f$) *vs* [DNA] plots based on eq iii (Figure S2). The K_b values of these complexes were observed to be 0.97×10^5, 0.053×10^5, and 7.7×10^5 M^{-1} (π−π*), respectively.

2.3.1.2. Ethidium Bromide Quenching Study. Ethidium bromide prominently displays emission after combining with DNA. Consequently, the competitive binding of these complexes (**7a**−**c**) to Ct-DNA was studied *via* the ethidium bromide displacement assay by computing the degree of quenching of the fluorescence intensity. Although the ethidium bromide dye is minimally fluorescent, its fluorescence varies immensely when intercalated with DNA. Other chemical moieties that can substitute EtBr in a competitive manner and bind to the same spot can extinguish the enhanced fluorescence.[33] Upon continuous addition of complexes with increasing concentration (5−60 μM), a regular decrease in the fluorescence intensity was perceived as EtBr was displaced from the EtBr−Ct-DNA adduct by the complexes and free EtBr is nonemissive in nature. In order to determine the K_{app} values, the concentrations of DNA and EtBr were derived from the literature as [EtBr] = 8 μM and [DNA] = 120 μM. Based on this hypochromic shift, we plotted a linear graph using the I_0/I vs the concentration of these complexes. Then, using eq vi, K_{app} values of the complexes **7a**, **7b**, and **7c** were calculated as 0.2×10^7, 0.14×10^7, and 1.6×10^6 M^{-1}, respectively, under 50% quenched conditions, whereas the value of K_{EtBr} reported in the literature is 1.0×10^7 M^{-1} (Figure S3, Table 2). The

Table 2. Binding Parameters for the Interaction of ct-DNA and Complexes (7a−c)

complex	λ_{max} (nm)	$\Delta\epsilon^a$ (%)	$K_b{}^b$ (M^{-1})	$K_{SV}{}^c$ (M^{-1})	$K_{app}{}^d$ (M^{-1})
7a	340	22.49	0.97×10^5	1×10^4	0.2×10^7
7b	350	46.66	0.053×10^5	4×10^3	0.14×10^7
7c	330	27.12	7.7×10^5	8.2×10^3	0.19×10^7

[a]Change in molar absorptivity. [b]Intrinsic DNA-binding constant. [c]Stern−Volmer quenching constant. [d]Apparent DNA-binding constant.

Stern−Volmer quenching constant (K_{SV}) was calculated using eq v (Figure S3), and the values were found to be 1×10^4 M^{-1} for **7a**, 4×10^3 M^{-1} for **7b**, and 8.2×10^3 M^{-1} for **7c** (Table 2). From these values, it was obvious that complex **7a** exhibited the maximum K_{app}, validating the most efficient intercalation of this complex compared to the other two complexes.

2.3.1.3. BSA Binding Studies. The reactivity of chemical and biological systems *in vitro* can be easily identified *via* fluorescence spectroscopy. It provides nonintrusive measurements of compounds in low concentrations under physiological settings.[34] The difference in the fluorescence intensity can be used to determine the type of binding. Fluorescence quenching is the loss of fluorescence intensity caused by a change in the environment surrounding the fluorophore.[35] Serum albumin plays a vital role as a transporter in the cellular environment. Bovine serum albumin (BSA) is a structural homolog of human serum albumin (HSA) and is used in tryptophan quenching experiments. The fluorescence spectra of BSA were verified in the absence and presence of complexes by fitting the excitation wavelength at 280 nm, and hence, the emission was observed at 340 nm. Thus, the normal fluorescence intensity of BSA was quenched and showed a hypochromic shift upon the gradual addition of complexes from 0 to 20 μM. The binding of complexes (**7a**−**c**) with BSA significantly quenched the fluorescence intensity of BSA, and it was linked to an increase in the hydrophobicity of the area surrounding the tryptophan residues in BSA.[36] The steady decrease in the fluorescence intensity indicated that these types of complexes were very efficient in binding with BSA, which was determined by the Stern−Volmer quenching constant (K_{HSA}), quenching rate constant (K_q), and binding constant (K) by applying eqs vii and viii (Figure S4). We obtained the values of K_{BSA} as 0.137×10^6 M^{-1} for **7a**, 0.201×10^6 M^{-1} for **7b**, and 0.296×10^6 M^{-1} for **7c**. After that, the bimolecular quenching constant (K_q) was calculated with the help of K_{BSA} and the tryptophan lifetime in BSA ($\tau_0 = 1 \times 10^{-8}$ s), and thus, we acquired the values of K_q as 1.3×10^{13} $M^{-1}S^{-1}$ for **7a**, 2.01×10^{13} $M^{-1}S^{-1}$ for **7b**, and 2.9×10^{13} $M^{-1}S^{-1}$ for **7c**, which were superior to the maximum potential value of dynamic quenching (2×10^{10} $Lmol^{-1}s^{-1}$) because of molecular collision. Consequently, the experimental K_q values of these complexes indicated a static quenching pathway and the higher order (10^{13}) of biomolecular quenching constant (K_q) indicated the noteworthy biomolecular quenching in overtone with biomolecular binding. Similarly, the binding affinity (K) and number of binding sites (n) were determined from the Scatchard plots using eq viii (Figure S4). The binding affinities (K's) obtained for complexes **7a**, **7b**, and **7c** were 0.07×10^6, 0.057×10^6, and 0.087×10^4 M^{-1}, respectively. Instead, the number of binding sites (n) was calculated as 0.8, 1.33, and 1.21 for complexes **7a**, **7b**, and **7c**, respectively (Table 3).

Table 3. Binding Parameters for the Interaction of Complexes (7a−c) and BSA

complex	K_{BSA} (M^{-1})[a]	k_q (M^{-1} s^{-1})[b]	K (M^{-1})[c]	n[d]
7a	0.137×10^6	1.3×10^{13}	0.070×10^6	0.8
7b	0.201×10^6	2.01×10^{13}	0.057×10^6	1.33
7c	0.296×10^6	2.9×10^{13}	0.087×10^6	1.21

[a]Stern−Volmer quenching constant. [b]Quenching rate constant. [c]Binding constant with BSA. [d]Number of binding sites.

2.3.1.4. Cytotoxicity Assay. To determine the *in vitro* cytotoxicity, an MTT assay was performed for the synthesized complexes (**7a**−**c**) at 0−125 μM concentrations with 48 h incubation in a CO_2 incubator. The cancer cell lines used for toxicity evaluation were HeLa, MCF-7, U87MG, and a non-cancer human embryonic kidney cell line, HEK293. Complex **7a** had a good cytotoxicity profile in comparison with other complexes (Figure S5, Table 4). In addition, the selectivity factor was higher in the case of complex **7a** compared to the other synthesized complexes (**7b** and **7c**). We conclude from the cytotoxicity data that the higher the lipophilicity of complexes, the better the permeability inside the cells, which enhanced their anticancer activity. Complex **7a** has a lipophilic value of around 0.9, whereas the other complexes **7b** and **7c** have lipophilic values of around 0.5 and 0.3. Complex **7a** served as a cytoselective complex among all other synthesized complexes along with cisplatin (positive control).

2.3.1.5. Cellular Localization Study. A colocalization study was performed with the most potent complex **7a** using the

https://doi.org/10.1021/acsomega.3c01639
ACS Omega 2023, 8, 32382−32395

Table 4. Cytotoxicity Profile of Synthesized Complexes 7a−c

	IC_{50} (μM)[a]				selectivity factor[f]		
complex	HeLa[b]	MCF 7[c]	U87MG[d]	HEK293[e]	HeLa	MCF-7	U87MG
7a	7.68 ± 1.2	7.85 ± 3.09	63.33 ± 2.6	85.56 ± 2.5	11.68	10.89	1.35
7b	15.84 ± 0.7	40.89 ± 1.8	>100	>100	6.31	2.45	1
7c	19.40 ± 0.19	40.93 ± 1.4	76.01 ± 3.5	>100	5.15	2.44	1.31
cisplatin	16.40 ± 0.16	20.12 ± 1.6	16.87 ± 2.1	34.78	2.07	1.68	2.01

[a]IC_{50}: concentration at which 50% of the cells undergo cell death. [b]Human epitheloid cervix carcinoma cancer cell lines. [c]Human breast cancer cell line. [d]Human glioma cancer cell line. [e]Human embryonic kidney 293 cells. [f]Ratio of IC_{50} between the HEK-293 and all cancer cells.

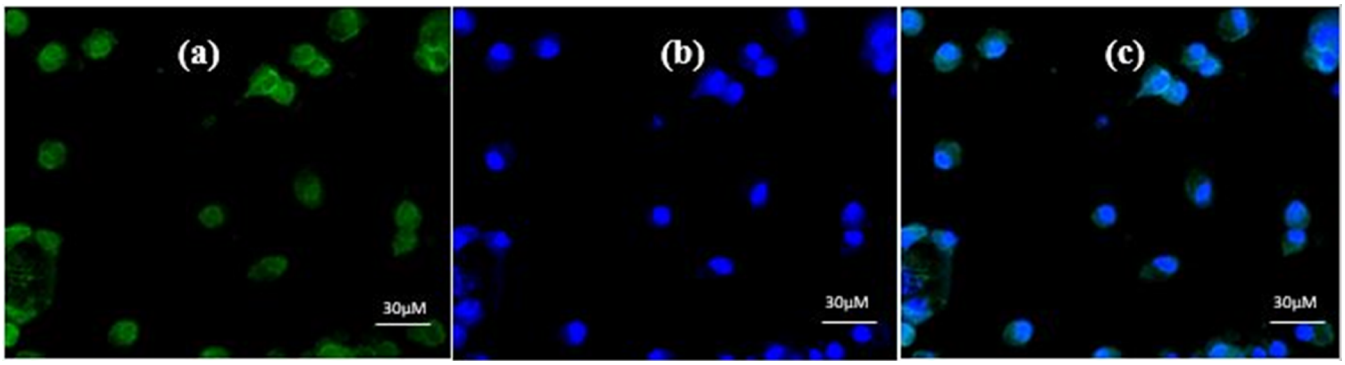

Figure 2. Confocal imaging of complex **7a** at the IC_{50} value in the U87MG cell line: (a) blue filter, (b) DAPI filter, and (c) merged image.

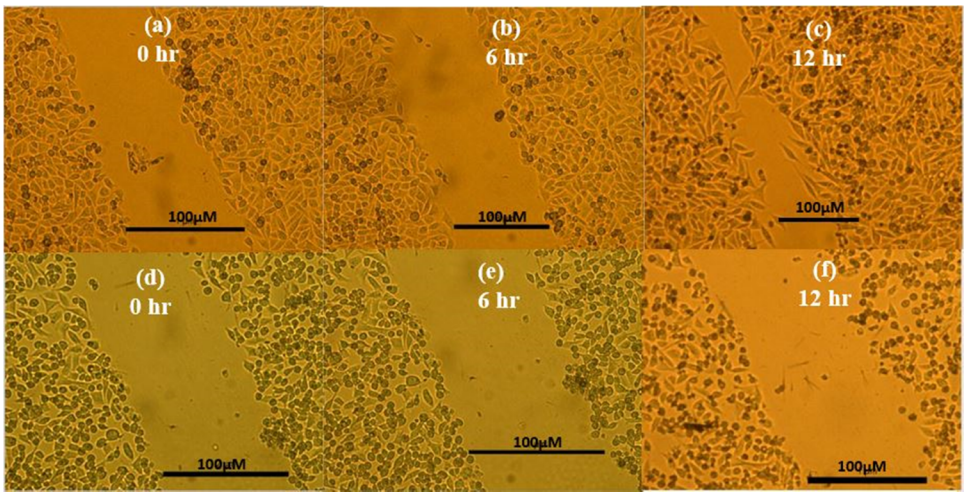

Figure 3. Scratch wound healing assay of control (a−c) and HeLa cells treated with complex **7a** (d−f).

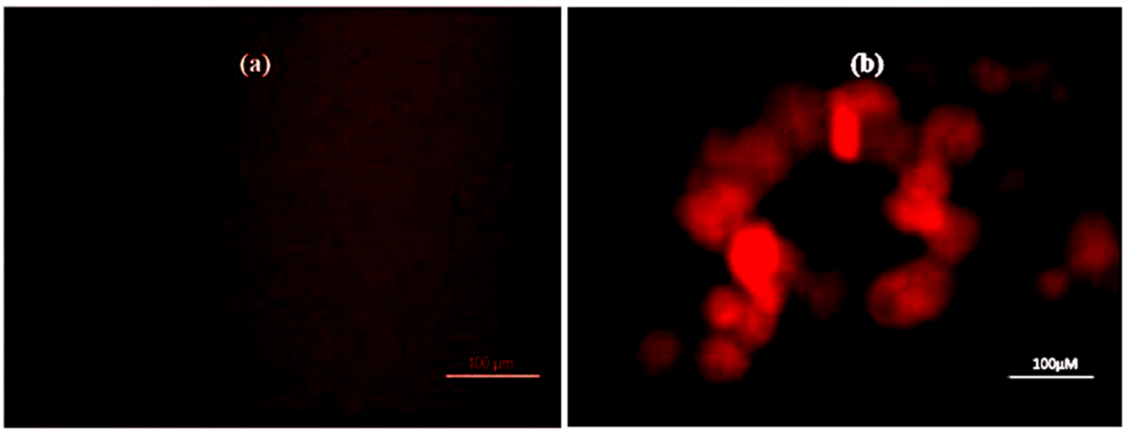

Figure 4. ROS of MCF-7: (a) control and (b) HeLa cells treated with IC_{50} concentration of complex **7a**.

https://doi.org/10.1021/acsomega.3c01639
ACS Omega 2023, 8, 32382−32395

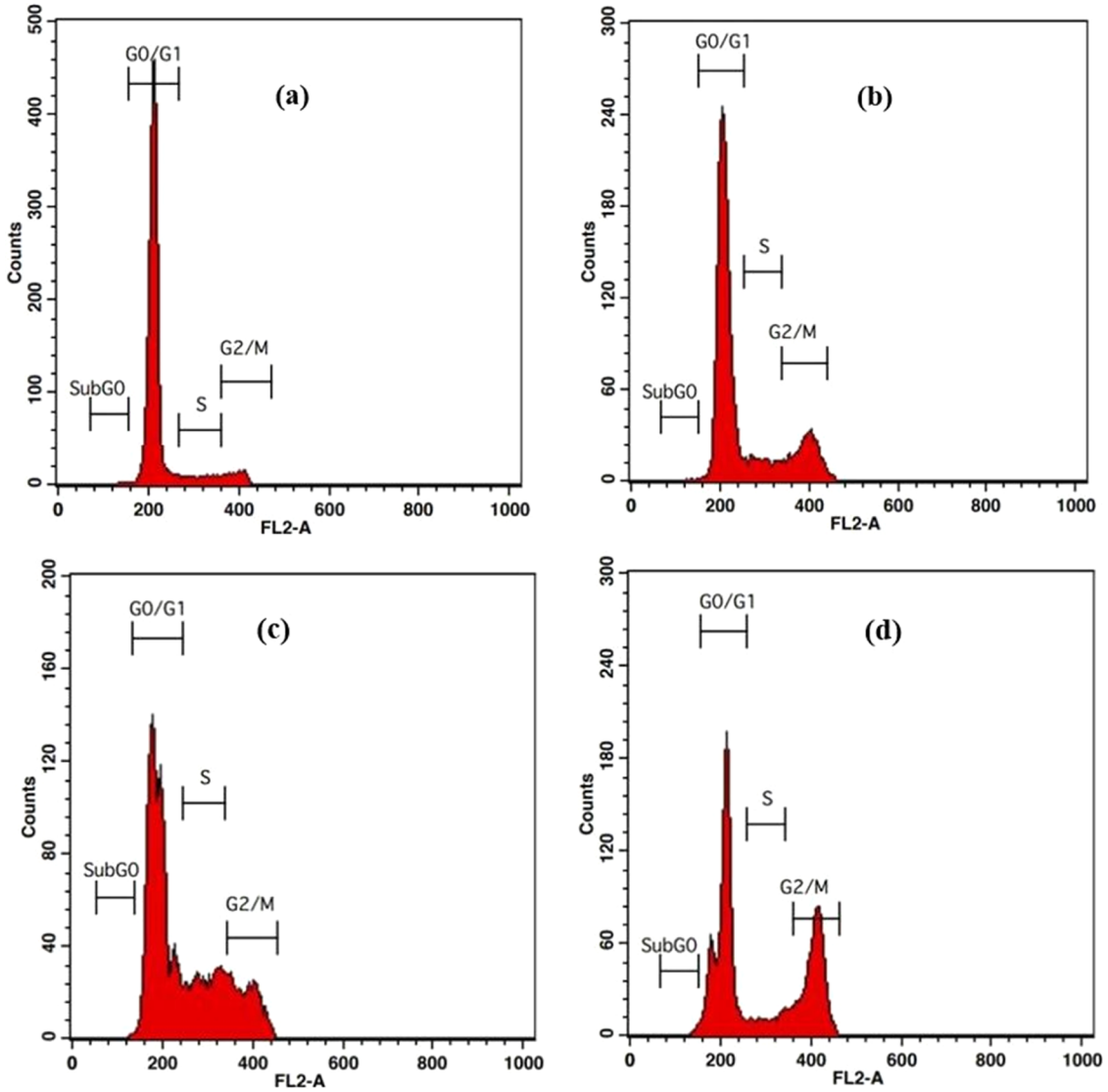

Figure 5. Cell cycle analysis of MCF-7: (a) control, (b) with 4 μM complex **7a**, (c) with 8 μM complex **7a**, and (d) with colchicine (15 μM).

U87MG cell line. It was stained with the nucleus-staining dye DAPI and visualized for imaging studies *via* a confocal laser scanning microscope (CLSM 510, Zeiss, Oberkochen, Germany). DAPI mainly stains the nucleus blue, whereas complex **7a** stains the nuclei green. A DAPI filter was used to observe DAPI-stained nuclei, and a blue filter was used to detect the staining of complex **7a**. The colocalization of this complex in the nucleus confirmed the intracellular distribution of this complex mostly in the nucleus (Figure 2).

2.3.1.6. Scratch Wound Healing Assay. Metastasis is a salient feature of cancer cells. In order to study the migration of cells, a scratch wound healing assay was performed by a 2D method. Initially, a gap was created by scratching a monolayer of cells, and its ability to migrate and heal the gaps was studied.[37] The control HeLa cells were capable of migrating near the wounded site and minimizing the gap between them, as shown in Figure 3 at the 0-, 12-, and 24-h intervals, whereas HeLa cells treated with the IC_{50} concentration of complex **7a** could not close the gaps; instead, the cell density decreased, generating larger gaps than the original wounded site. This result indicates that complex **7a** inhibits the metastasis of HeLa cancer cells.

2.3.1.7. Detection of ROS Generation by the DCFDA Staining Assay. Most chemotherapeutics increase intracellular levels of reactive oxygen species (ROS), and many can alter the redox homeostasis of cancer cells. It is widely accepted that the anticancer effect of these chemotherapeutics is due to the induction of oxidative stress and ROS-mediated injury in cancer cells. As intracellular ROS can control the apoptotic effect, it was identified by means of a 2,7-dichlorodihydrofluorescein diacetate (DCFH-DA) assay. In the presence of ROS, this dye is transformed into a highly fluorescent complex (2′,7′-dichlorofluorescein, DCF). As shown in Figure 4, in the control experiment, no apparent fluorescence was observed. However, after the treatment of MCF-7 cells with complex **7a** at its IC_{50} value, followed by the addition of 10 μM DCFH-DA and incubation for 4 hr in a dark and humified atmosphere, a bright red fluorescence was observed. Thus, it was proved that ROS generation is caused by complex **7a** in MCF-7 cells.

2.3.1.8. Cell Cycle Analysis. MCF-7 cells were incubated with 4 and 8 μM concentrations of complex **7a**, and they were sequestered after 24 h for the cell cycle analysis. The results indicate that the G0/G1 phase gradually decreased with an increase in complex **7a** concentration in a dose-dependent

https://doi.org/10.1021/acsomega.3c01639
ACS Omega 2023, 8, 32382−32395

manner. In the case of the S and G2/M phases, there was a gradual increase in the concentration of cells in a dose-dependent manner. Furthermore, there was a decrease in the sub-G0 phase. In the sub-G0 phase, a small percentage of cells were present because the cells would have lost their DNA, so they do not appear in the sub-G0 area.[38] In the regulating processes of cell proliferation, the cell cycle and apoptosis play critical roles. Cell cycle checkpoints safeguard the dividing cells from the potentially harmful effects of DNA replication.[39] On the other hand, DNA damage has catastrophic repercussions. The detection of DNA damage by the checkpoints in the S and G2/M phases prevents cells from undergoing the cell cycle or the cells die by apoptosis. This event causes the disappearance of cells in the sub-G1 area.[39] For many chemotherapeutic compounds, the G2/M arrest checkpoint is the potential target. The G2/M arrest checkpoint might allow cells containing damaged DNA to enter the mitosis phase and they undergo apoptosis. Complex **7a** blocks the S and G2/M phases of 10.07, 22.61, and 18.48%, 17.15% respectively. This result indicates that cells undergo both S and G2/M phase arrest (Figure 5, Table 5).

Table 5. Different Phases of Cell Cycle Analysis of Control and Treated MCF-7 Cells

sample	sub-G0	G0/G1	S	G2/M
control	0.24	87.72	6.36	5.91
7a (4 μM)	0.16	71.23	10.07	18.48
7a (8 μM)	0.08	59.57	22.61	17.15
colchicine (8 μM)	0.64	54.11	8.30	34.60

2.3.1.9. Apoptosis in MCF-7 Cells and the Annexin FITC/PI Assay. The cell death by complex **7a** *via* apoptosis was monitored by the changes in phosphatidylserine using Annexin V FITC. Apoptosis was quantified by annexin V FITC binding to exposed PS on the outer surface of the membrane. Equal proportions of annexin V FITC and propidium iodide were added. In viable cells, phosphatidylserine is generally located inside the cell; when an apoptotic event occurs, it is translocated outside to the plasma membrane. Hence, it can easily be quantified by annexin V FITC.[40] PI inclusion enables one to distinguish the cells as viable ($AnnV^-/PI^-$), early apoptotic ($AnnV^+/PI^-$), late apoptotic ($AnnV^+/PI^+$), and necrotic ($AnnV^-/PI^+$).[41] Flow cytometry results showed the shift of the cell population from viable to apoptotic after treatment with complex **7a**. Treating with complex **7a** at concentrations of 4 and 8 μM induced 13.18 and 8.68% early apoptosis, 5.90 and 15.35% late apoptosis, and 5.73 and 10.48% necrosis in MCF-7, respectively (Figure 6, Table 6).

4. CONCLUSIONS

In summary, the CuAAC "click"-derived synthesis of three complexes (**7a**–**c**) was accomplished, and cytotoxic screening with three different cancer cell lines along with one normal cell line was performed. Detailed investigations confirmed that the cytotoxic behavior of complex **7a** was very effective against all cancer cell lines compared to Ir(III) and Re(I) complexes. Complex **7a** exhibited significant cytoselectivity in all of the cancer cell lines compared to complexes **7b** and **7c** and cisplatin. However, both of the complexes (**7a**, **7c**) displayed excellent binding ability toward DNA. Surprisingly, all three complexes showed excellent binding efficacy against BSA. The subcellular localization study showed that the complex was confined in the nucleus and hence resulted in nuclear DNA intercalation. Moreover, the generous production of ROS upon treatment with complex **7a** led to the initiation of oxidative stress and ROS-mediated injury in MCF-7 cells. The Annexin V FITC/PI test confirmed the lethal capacity of complex **7a** on MCF-7 cancer cells by causing apoptosis, which could most probably be a result of cellular energy stress induced by the higher degree of ROS production and DNA damage. Concomitantly, complex **7a** played a significant role in both S and G2/M phases of cell cycle arrest in MCF-7 cells at the verified concentrations of 4 and 8 μM. In a nutshell, we envision complex **7a** as a potential therapeutic agent against HeLa, MCF-7, and U87MG cell lines.

5. EXPERIMENTAL SECTION

5.1. Materials and Methods. In this work, commercial-quality reagents and solvents were used. All of the chemicals and biochemicals were procured from Sigma-Aldrich Chemical Ltd, Merck. All cell lines were purchased from NCCS, Pune. DMEM medium, 1% penicillin, streptomycin, and 1% Glutmax were bought from Gibco. 10% Fetal bovine serum and 0.25% trypsin-EDTA were obtained from Himedia and Thermo Fisher Scientific, respectively. NMR spectra were recorded on a 400 MHz Advance Bruker DPX spectrometer with tetramethylsilane (TMS) as the internal standard. An Elchem Microprocessor-based DT apparatus was used to measure the melting points of the complexes. Infrared (IR) spectra were recorded on a Shimadzu Affinity FT-IR spectrometer in the range of 4000–400 cm^{-1}. The mass spectra of the synthesized compounds were recorded on Applied Biosystems (API-4000 ESI-mode), using methanol as the solvent. UV–visible and fluorescence spectra were recorded on a JASCO V-760 spectrometer and Hitachi F7000 fluorescence spectrophotometer, respectively. A TDS conductometer was used to measure the conductivity. An Elisa reader and 96-well plates were used for the MTT assay.

5.2. Chemistry. *5.2.1. Synthesis and Characterization. 5.2.1.1. Synthesis of Benzothiazolylphenol (**3**).* Initially, equimolar amounts (1:1) of 2-amino thiophenol (**1**) and 2-hydroxy benzaldehyde (**2**) were taken in a round-bottom flask and dissolved in ethanol. It was then refluxed at 80 °C in an oil bath for 12 h. The reaction was closely supervised by TLC using a hexane/ethyl acetate solvent system with a 3:1 ratio. After completion of the reaction, the solution was transferred to a clean beaker and air-dried. White needle-like crystals of benzothiazolylphenol compounds were obtained with 95% yield.

*5.2.1.2. 2-(Benzo[d]thiazol-2-yl)phenol (**3**).* Yield: 95%; color: white needle-like crystals; R_f [hexane/ethyl acetate (3:1)]: 0.72; ^1H NMR (400 MHz, $CDCl_3$) σ 6.96 (t, J = 7.6 Hz, 1H), 7.11 (d, J = 8.0 Hz, 1H), 7.36–7.42 (m, 2H), 7.51 (t, J = 8.0 Hz, 1H), 7.70 (d, J = 8.0 Hz, 1H), 7.90 (d, J = 8.0 Hz, 1H), 8.00 (d, J = 8 Hz, 1H), 12.52 (s, 1H, OH).

*5.2.1.3. Synthesis of 2-(2-(4-Bromobutoxy)phenyl)benzo[d]thiazole (**4**).* The compound benzothiazolylphenol (**3**) was taken in a round-bottom flask for the next step and dissolved in dichloromethane. To this, 10% NaOH was added and stirred for a few minutes. A catalytic amount of tributyl ammonium bromide (TBAB) was added to the reaction mixture and stirred for about 10 min. After that, 1,4 dibromo butane (1:8) was added into the round-bottom flask, and the reaction was continued for another 1 h with stirring at ambient temperature. The evolution of the reaction was monitored by thin-layer

https://doi.org/10.1021/acsomega.3c01639
ACS Omega 2023, 8, 32382–32395

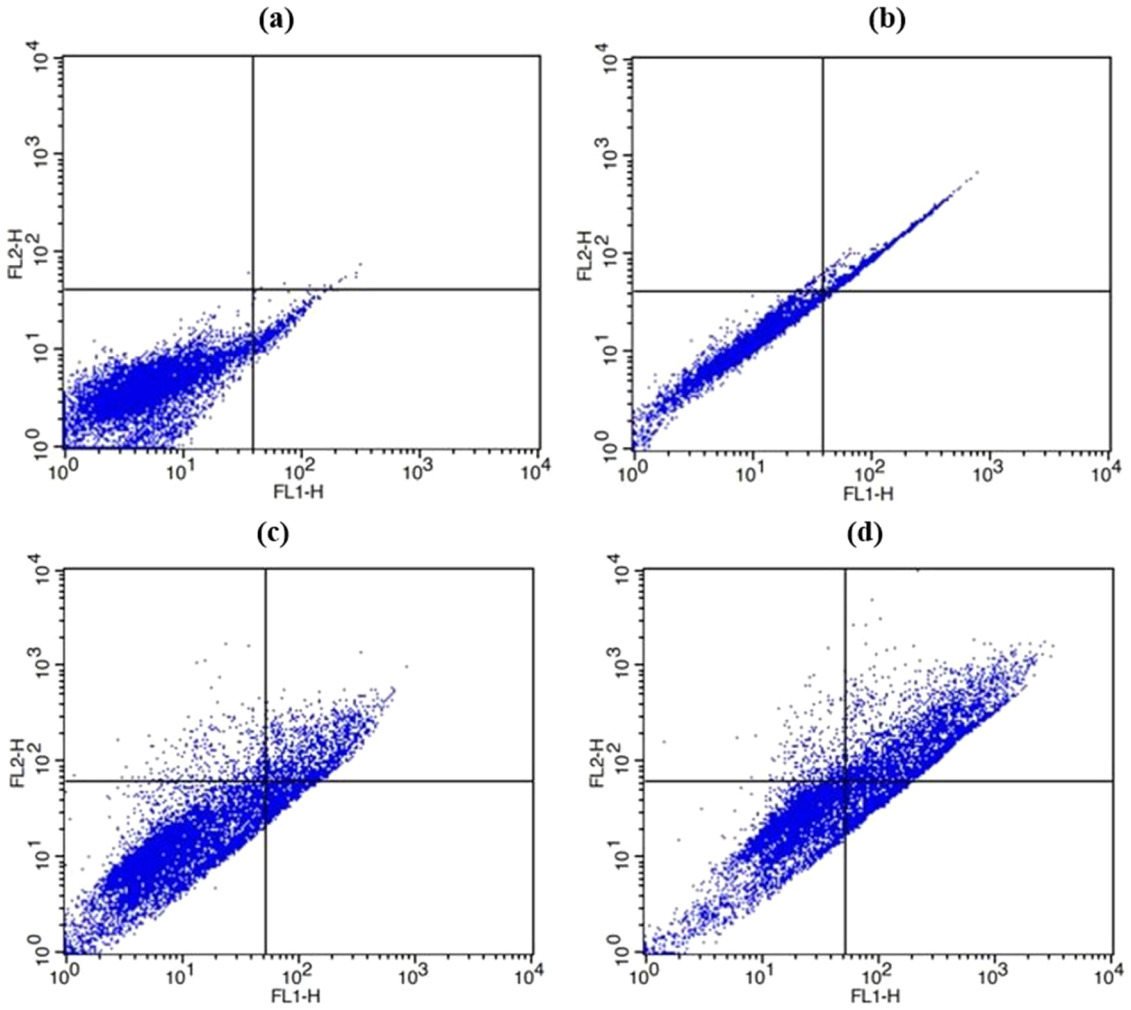

Figure 6. Apoptosis assay of MCF-7: (a) control, (b) with 4 μM complex **7a**, (c) with 8 μM complex **7a**, and (d) with 15 μM cisplatin.

Table 6. Apoptosis Assay of Control and Treated MCF-7 Cells

sample	viable cells (%)	early apoptosis (%)	late apoptosis (%)	necrotic cells (%)
control	93.77	2.47	1.14	2.62
7a (4 μM)	75.19	13.18	5.90	5.73
7a (8 μM)	65.49	8.68	15.35	10.48
cisplatin (15 μM)	52.84	12.00	32.04	3.12

chromatography (TLC) using a hexane/ethyl acetate solvent system at a 3:1 ratio. After completion of the reaction, the reaction mixture was transferred to a separating funnel, and the aqueous and organic layers were distinguished. The organic layer was separated and collected in a beaker, and anhydrous sodium sulfate was added to remove water from the organic layer (DCM). The DCM solvent containing the product was air-dried thoroughly. Purification of the crude compound was performed by column chromatography using hexane as a mobile phase. A colorless oily (semisolid) compound 2-(2-(4-bromobutoxy)phenyl)benzo[*d*]thiazole (**4**) was isolated with excellent yield (92%).

*5.2.1.4. 2-(2-(4-Bromobutoxy)phenyl)benzo[d]thiazole (**4**).* Yield: 92%; color: square-shaped white crystals; R_f [hexane/ethyl acetate (3:1)]: 0.82; ^{1}H NMR (400 MHz, $CDCl_3$): σ 2.19−2.24 (m, 4H, -CH_2), 3.6 (t, J = 5.6 Hz, 2H, -CH_2), 4.25 (t, J = 5.6 Hz, 2H, -CH_2), 7.03 (d, J = 8.4 Hz, 1H, ArH), 7.15 (t, J = 7.2 Hz, 1H, ArH), 7.40 (t, J = 7.6 Hz, 1H, ArH), 7.42−7.52 (m, 2H, ArH), 7.95 (d, J = 8.0 Hz, 1H), 8.10 (d, J = 8.0 Hz, 1H), 8.55 (d, J = 9.2 Hz, 1H); ^{13}C NMR (100 MHz, $CDCl_3$): σ 27.9 (CH_2), 29.6 (CH_2), 33.5 (CH_2), 68.1 (CH_2), 112.2 (CH), 121.2 (CH), 121.3 (CH), 122.28 (C), 122.81 (CH), 124.64 (CH), 125.59 (CH), 129.74 (CH), 131.78 (CH), 136.02 (C), 152.12 (C), 156.46 (C), 163.01 (C).

*5.2.1.5. Synthesis of 2-(2-(4-Azidobutoxy)phenyl)benzo-[d]thiazole (**5**).* The compound 2-(2-(4-bromobutoxy)-phenyl)benzo[*d*]thiazole (**4**) was then reacted with sodium azide (NaN_3) in a 1:4 molar ratio in tetrahydrofuran (THF) solvent at room temperature while stirring for 48 h. After 48 h, the reaction mixture was transferred to a clean beaker and air-dried to obtain 2-(2-(4-azidobutoxy)phenyl)benzo[*d*]thiazole with excellent yield (96%).

*5.2.1.6. 2-(2-(4-Azidobutoxy)phenyl)benzo[d]thiazole (**5**).* Yield: 92%; color: light brown; R_f [hexane/ethyl acetate (3:1)]: 0.65; ^{1}H NMR (400 MHz, $CDCl_3$): σ 1.85−1.92 (m, 2H, CH_2), 2.00−2.05 (m, 2H, CH_2), 3.34 (t, J = 6.4 Hz, 2H, CH_2), 4.16 (t, J = 6.0 Hz, 2H, CH_2), 6.95 (d, J = 8.4 Hz, 1H, ArH), 7.05 (t, J = 7.6 Hz, 1H, ArH), 7.29 (t, J = 7.6 Hz, 1H, ArH), 7.36 (t, J = 7.2 Hz, 1H, ArH), 7.41 (t, J = 7.2 Hz, 1H, ArH), 7.86 (d, J = 7.6 Hz,1H, ArH), 8.01 (d, J = 7.22 Hz,1H, ArH), 8.46 (d, J = 8.0 Hz, 1H, ArH); ^{13}C NMR (100 MHz,

https://doi.org/10.1021/acsomega.3c01639
ACS Omega 2023, 8, 32382−32395

$CDCl_3$): σ 26.1 (aliphatic CH_2), 30.3 (aliphatic CH_2), 51.2 (aliphatic CH_2), 68.5 (aliphatic CH_2), 112.1 (CH), 121.18 (CH), 121.32 (CH), 122.23 (C), 122.78 (CH), 124.66 (CH), 125.98 (CH), 129.73 (CH), 131.81 (CH), 136.01 (C), 152.09 (C), 156.46 (C), 163.01 (C).

*5.2.1.7. Synthesis of 2-(2-(4-(4-(Pyridin-2-yl)-1H-1,2,3-triazol-1-yl)butoxy)phenyl)benzo[d]thiazole (**6**).* Compound **5** was reacted with 2-ethenyl pyridine (1:1) *via* the click reaction using copper sulfate pentahydrate ($CuSO_4$, $5H_2O$) and sodium ascorbate as reducing agents dissolved in methanol and subjected to a microwave reaction at 50 watts (80 °C) for 15 min. The reaction mixture was then carefully monitored by thin-layer chromatography (TLC) using 100% methanol as the solvent system. After completion of the reaction, the reaction mixture was filtered using Whatman filter paper and air-dried followed by recrystallization from a methanol/diethyl ether mixture to obtain the compound 2-(2-(4-(4-(pyridin-2-yl)-1*H*-1,2,3-triazol-1-yl)butoxy)phenyl)benzo[*d*]thiazole (**6**) with excellent yield (94%).

*5.2.1.8. 2-(2-(4-(4-(Pyridin-2-yl)-1H-1,2,3-triazol-1-yl)-butoxy)phenyl)benzo[d]thiazole (**6**).* Yield: 92%; color: dirty white; R_f: [methanol 100%] 0.32; ^{1}H NMR (400 MHz, $CDCl_3$) δ 2.00 (t, J = 6.00 Hz, 2H, CH_2), 2.29 (t, J = 7.60 Hz, 2H, CH_2), 4.17 (t, J = 5.60 Hz, 2H, CH_2), 4.52 (t, J = Hz, 2H, CH_2), 6.95 (d, J = 8.40 Hz, 2H, ArH), 7.05 (t, J = 7.20 Hz, 1H, ArH), 7.29 (t, J = 7.20 Hz, 1H, ArH), 7.36 (t, J = 7.60 Hz, 1H, ArH), 7.41 (t, J = 7.60 Hz, 1H, ArH), 7.72 (t, J = 7.60 Hz, 1H, ArH), 7.91 (d, J = 7.60 Hz, 1H, ArH), 8.01 (d, J = 8.00 Hz, 1H, ArH), 8.14 (t, J = 7.60 Hz, 2H, ArH), 8.45 (d, J = 8.00 Hz, 1H, ArH); ^{13}C NMR (100 MHz, $CDCl_3$): δ 26.2 (aliphatic CH_2), 37.4 (aliphatic CH_2), 50.1 (aliphatic CH_2), 68.1 (aliphatic CH_2), 112.17 (CH peak), 121.28 (CH peak), 121.43 (CH peak), 122.01 (CH peak), 122.25 (CH peak), 122.75 (C peak), 122.76 (CH peak), 124.67 (CH peak), 125.98 (CH peak), 131.81 (CH peak), 135.91 (C peak), 136.95 (C peak), 152.08 (C peak), 156.31 (C peak), 162.87 (C peak); ESI-MS (MeOH): m/z = 428.4 $[M + H]^+$.

*5.2.1.9. Synthesis of the 2-(2-(4-(4-(Pyridin-2-yl)-1H-1,2,3-triazol-1-yl)butoxy)phenyl)benzo[d]thiazole-Ruthenium (II) Arene Complex (**7a**).* Accurately, 15 mg of ligand **6** (0.035 mmol, 1 equiv) was dissolved in methanol (10 mL). Then, 10 mg of $[Ru^{II}(\eta^6\text{-}p\text{-cym})(Cl)_2]_2$ (0.017 mmol, 0.5 equiv) was added to the same solution, and the reaction mixture was continuously stirred at room temperature for 2 h. After completion of the reaction, as confirmed by TLC, the solvent was evaporated, yielding a brown-colored crude mass, which was washed several times with hexane and diethyl ether. The crude product was purified by crystallization from a diethyl ether/methanol (1:1) solvent system, which yielded an 84% pure crystalline product of complex **7a**.

*5.2.1.10. [(η^6-p-Cymene)Ru^{II}(Cl)(K^2-N,N-(2-(4-(4-(pyridin-2-yl)-1H-1,2,3-triazol-1-yl)butoxy)phenyl)benzo[d]thiazole-Ruthenium)]Cl (**7a**).* 20 mg (0.027 mmol); yield: 84%; color: brown; Mp: 170−172 °C; R_f [100% methanol]: 0.22; FT-IR (cm^{-1}): C═N peak (1627), CH_3 (C-H) asymmetric stretch (2958), symmetric stretch (2852), CH_3 (C-H) asymmetric bend (1442); ^{1}H NMR (400 MHz, DMSO-d_6): δ 0.86 (d, J = 6.8 Hz, 3H, *p*-cymene CH_3), 0.94 (d, J = 6.8 Hz, 3H, *p*-cymene CH_3), 2.29 (s, 3H, *p*-cymene CH_3), 2.78−2.86 (m, *p*-cymene CH), 4.37 (brs, 2H, CH_2), 4.83 (brs, 2H, CH_2), 5.75−5.94 (m, 4H, CH_2), 6.06 (d, J = 6 Hz, 1H, *p*-cymene CH), 6.07−6.10 (m, 3H, *p*-cymene CH), 7.17 (t, J = 7.2 Hz, 1H, ArH), 7.31 (d, J = 8.4 Hz, 1H, ArH), 7.40 (t, J = 7.6 Hz, 1H, ArH), 7.50−7.57 (m, 2H, ArH), 7.68 (t, J = 6 Hz, 1H, ArH), 8.03−8.06 (m, 2H, ArH), 8.15−8.24 (m, 2H, ArH), 8.44 (d, J = 7.6 Hz, 1H, ArH), 9.29 (s, 1H, ArH), 9.45 (d, J = 5.2 Hz, 1H, ArH); ^{13}C NMR (100 MHz, DMSO-d_6): δ 18.60 (CH), 21.5 (CH_3), 22.3 (CH_3), 26.0 (CH_2), 26.9 (CH_2), 30.8 (CH), 52.2 (CH_2), 68.7 (CH_2), 83.3 (C), 83.8 (C), 85.1 (C), 86.2 (C), 102.8 (C), 104.0 (C), 113.7 (CH), 121.6 (CH), 122.3 (CH), 122.7 (CH), 122.8 (CH), 125.4 (CH), 126.1 (CH), 126.4 (CH), 127.8 (CH), 132.9 (CH), 135.8 (C), 140.7 (CH), 146.4 (C), 148.3 (C), 152.0 (C), 156.2 (C), 156.6 (CH); ESI-MS (MeOH): m/z = 698.13 $[M - Cl]^+$; HRMS (MeOH): m/z: 698.1294 (calculated), 698.1315 (found) $[M - Cl]^+$.

*5.2.1.11. Synthesis of the 2-(2-(4-(4-(Pyridin-2-yl)-1H-1,2,3-triazol-1-yl)butoxy)phenyl)benzo[d]thiazole−Iridium (III) Chloride Complex (**7b**).* Exactly, 15 mg of ligand **6** (0.035 mmol, 1 equiv) was dissolved in methanol (10 mL). Then, 14 mg of $[Ir^{III}(cp^*)(Cl)_2]_2$ (0.017 mmol, 0.5 equiv) was added to the same solution, and the reaction mixture was continuously stirred at room temperature for 2 h. Finally, the solvent was evaporated and the obtained crude product was further crystallized from a diethyl ether/methanol (1:1) solvent system, which yielded an 88% pure crystalline product of complex **7b**.

5.2.1.12. [(η^5-Cp)Ir^{III}Cl(K^2-N,N-2(2-(4-(4-(Pyridin-2-yl)-1H-1,2,3-triazol-1-yl)butoxy)phenyl)benzo[d]thiazole)]Cl (**7b**).* 22 mg (0.025 mmol); yield: 88%; color: dark red; Mp: 174−176 °C; R_f [100% methanol]: 0.24; FT-IR (cm^{-1}): 1632 (C═N peak), 257 (CH_3 (C-H) asymmetric stretch), 2851 (CH_3 (C-H) symmetric stretch), 1448 (CH_3 (C-H) asymmetric bend); ^{1}H NMR (400 MHz, DMSO-d_6): δ 1.63 (s, 15H, Cp*), 2.06 (t, 2H, J = 6.8 Hz, CH_2), 2.31 (t, 2H, J = 6.8 Hz, CH_2), 4.39 (brs, 2H, CH_2), 4.87 (t, 2H, J = 6.4 Hz, CH_2), 7.16 (t, 1H, J = 7.2 Hz, ArH), 7.32 (t, 1H, J = 8.4 Hz, ArH), 7.39 (t, 1H, J = 7.6 Hz, 1H), 7.50−7.55 (m, 2H, ArH), 7.73 (t, 2H, J = 6.4 Hz, ArH), 8.00−8.06 (m, 2H, ArH), 8.30 (d, 1H, J = 7.6 Hz, ArH), 8.36 (d, 1H, J = 7.6 Hz, ArH), 8.45 (d, 1H, J = 7.6 Hz, ArH), 8.93 (d, 1H, J = 5.2 Hz, ArH), 9.45 (s, 1H, ArH); ^{13}C NMR (100 MHz, DMSO-d_6): δ 8.7 (3xCH_3), 9.8 (2xCH_3), 26.1 (CH_2), 26.8 (CH_2), 52.2 (CH_2), 68.7 (CH_2), 89.1 (C), 89.2 (CH), 113.7 (CH), 121.5 (C), 121.6 (CH), 122.7 (CH), 122.9 (CH), 125.3 (CH), 126.8 (CH), 127.8 (CH), 129.2 (CH), 132.9 (CH), 135.7 (C), 141.1 (CH), 141.7 (C), 148.4 (C), 151.9 (C), 152.8 (CH), 156.6 (C), 162.61 (C); ESI-MS (MeOH): m/z = 790.2 $[M - Cl]^+$; HRMS (MeOH): m/z: 790.1958 (calculated), 790.2019 (found) $[M - Cl]^+$.

*5.2.1.13. Synthesis of the 2-(2-(4-(4-(Pyridin-2-yl)-1H-1,2,3-triazol-1-yl)butoxy)phenyl)benzo[d]thiazole-Rhenium Tricarbonyl Complex (**7c**).* Initially, 15 mg of ligand **6** (0.035 mmol, 1 equiv) was dissolved in acetonitrile, and an equivalent amount of $Re^I(CO)_5Cl$ (0.035 mmol, 1 equiv) was added to it. Then, the reaction mixture was refluxed for 24 h. After completion of the reaction, the solvent was evaporated to obtain the crude complex, which was further crystallized from a diethyl ether/methanol (1:1) solvent system, which yielded a 90% pure crystalline product of complex **7c**.

*5.2.1.14. [Re^I(CO)$_3$Cl(K^2-N,N-2-(2-(4-(4-(Pyridin-2-yl)-1H-1,2,3-triazol-1-yl)butoxy)phenyl)benzo[d]thiazole)] (**7c**).* 28 mg (0.038 mmol); yield: 90%; color: brown; Mp: 181−183 °C; R_f [100% methanol]: 0.52; FT-IR (cm^{-1}): C═N (1594), CO stretch (2025, 1874). CH_2 (C-H) asymmetric stretch (2959), symmetric stretch (2855); ^{1}H NMR (400 MHz, DMSO-d_6): δ 9.27 (s, 1H), 1.97−2.00 (m, 2H, CH_2), 2.19−

https://doi.org/10.1021/acsomega.3c01639
ACS Omega 2023, 8, 32382−32395

2.25 (m, 2H, CH_2), 4.29 (t, J = 6 Hz, 2H, CH_2), 4.74 (t, J = 6.8 Hz, 2H, CH_2), 7.09 (t, J = 7.2 Hz, 1H, ArH), 7.23 (d, J = 8.4 Hz, 1H, ArH), 7.33 (t, J = 8 Hz, 1H, ArH), 7.43−7.49 (m, 2H, ArH), 7.58−7.60 (m,1H, ArH), 7.98 (d, J = 8.4 Hz, 2H, ArH), 8.17−8.24 (m, 2H, ArH), 8.38 (dd, J = 1.60, 8.00 Hz, 1H, ArH), 8.91 (d, J = 5.6 Hz, 1H, ArH), 9.27 (s, 1H, ArH); ^{13}C NMR (100 MHz, DMSO-d_6): δ 197.21 (2C, C═O), 192.28 (1C, C═O) 135.78 (1C), 156.66 (1C), 162.64 (1C), 26.2 (CH_2), 26.7 (CH_2), 51.8 (CH_2), 67.5 (CH_2), 113.7 (CH), 121.5 (CH), 122.3 (CH), 122.8 (CH), 123.1 (CH), 125.3 (CH), 126.3 (CH), 126.7 (CH), 126.9 (CH), 129.2 (CH), 132.9 (CH), 148.7 (CH), 153.5 (CH); ESI-MS (MeOH): m/z = 734.4 $[M + H]^+$; HRMS (MeOH): m/z: 734.1340 (calculated), 734.0625 (found) $[M + H]^+$.

5.3. UV/Fluorescence Study. Absorption and emission behaviors of all of these complexes were examined by a spectrofluorometric method in 10% DMSO solution.[42] The quantum yield (Φ) of all complexes was determined by the comparative William's method. Quinine sulfate was used as the reference fluorophore with excitation at 350 nm and emission at 452 nm; quantum yield (ΦR) = 0.50 in 1N H_2SO_4. The data attained and quantum yield value were determined according to eq i

$$\Phi_{Sample} = \Phi_{Reference} \times \frac{A_{Sample}}{A_{Reference}} \times \frac{(Abs)_{Reference}}{(Abs)_{Sample}} \times \frac{n_{Sample}^2}{n_{Reference}^2} \quad (i)$$

where φ is the quantum yield, A is the peak area, Abs is the absorbance at λ_{max}, n is the refractive index of the reference and sample, respectively. Quinine sulfate was applied as a standard. 0.5 M H_2SO_4 and water were used as solvents for the standard and synthesized compounds, respectively.

5.4. Lipophilicity Study Using the n-Octanol−Water Partition Coefficient (log $P_{o/w}$) by a UV Spectroscopic Method.[29] The hydrophobicity test was performed for the synthesized complexes employing the "shake-flask" method and the octanol−water phase partition coefficient. The complex was dissolved in a mixture of water and octanol, followed by shaking for 24 h. The mixture was then allowed to settle for over 30 min or centrifuged at 5000 rpm for 20 min. The resulting two phases were collected separately without cross-contamination of one solvent layer into another. The concentration of the complex in each phase was determined by UV−visible absorption spectroscopy at room temperature. The results given are the mean values obtained from three independent experiments. The concentration of the sample solution was used to calculate log $P_{o/w}$. Partition coefficients for all complexes were calculated using eq ii.

$$\log P_{o/w} = \log\left(\frac{[\text{complex in octane phase}]}{[\text{complex in aqueous phase}]}\right) \quad (ii)$$

5.5. Conductivity Measurement.[43] The conductivities of the complexes were determined using a conductivity-TDS meter-307 (Systronics, India) and a cell constant of 1.0 cm^{-1} due to the confirmed interaction of the complexes with DMSO and aqueous DMSO solution. For this experiment, we used a complex concentration of 3×10^{-5} M.

5.6. Biology. *5.6.1. Ct-DNA-Binding Assay.*[44] The UV absorbance titration study was accompanied by the successive addition of Ct-DNA from a fixed stock solution to a fixed complex concentration of 20 μM. Ct-DNA was dissolved in Tris-HCL buffer (5 mM Tris-HCl/50 mM NaCl in water, pH 7.4), and its absorbance was measured. The intrinsic binding constant (K_b) of the synthesized complexes was calculated from the equation given below (eq iii).

$$\frac{[DNA]}{(\varepsilon_a - \varepsilon_f)} = \frac{[DNA]}{(\varepsilon_b - \varepsilon_f)} + \frac{1}{K_b(\varepsilon_a - \varepsilon_f)} \quad (iii)$$

where [DNA] is the concentration of base pairs in Ct-DNA in the prepared stock solution, $\boldsymbol{\varepsilon}_a$ and $\boldsymbol{\varepsilon}_b$ are extinction coefficients of the apparently free complexes and fully bound complexes to Ct-DNA, respectively. The data were used to obtain $[DNA]/(\boldsymbol{\varepsilon}_a - \boldsymbol{\varepsilon}_f)$ *vs* [DNA] linear plots in Origin Pro 8.5. The intrinsic binding constant (K_b) was calculated from the linear fit by the ratio of the slope to the intercept. The percentage of hypochromic cells (% H) was calculated by eq ii

$$\%H = \frac{A_0 - A_F}{A_0} \times 100 \quad (iv)$$

A_0 is the absorption of the complex in the absence of Ct-DNA and A_F is the final value of absorption when there are no further changes in the absorption value with the addition of Ct-DNA to the complex.

5.6.2. Ethidium Bromide (EtBr) Displacement Assay.[44] EtBr, a well-known DNA intercalator, in its free form, is less fluorescent and its fluorescence intensity is enhanced when it binds to Ct-DNA. The binding capacity of these complexes toward Ct-DNA is calculated by quenching its fluorescence intensity. From the Stern−Volmer eq v, the Stern−Volmer quenching constant (K_{SV}) was calculated. The Stern−Volmer graph was obtained using I_0/I *vs* [complex], where I_0 and I are the emission intensities of EtBr−Ct-DNA in the absence and presence of a complex of concentration [Q], respectively, given the quenching constant (K_{SV}) using Origin Pro 8.5 software. Linear fit of the data was achieved by using the following equation.

$$\frac{I_0}{I} = 1 + K_{SV}[Q] \quad (v)$$

The apparent binding constant (K_{app}) of the synthesized complexes to Ct-DNA was calculated by plotting the fluorescence intensity versus complex concentration by using the following equation

$$K_{app} \times [\text{compound}]_{50} = K_{EtBr} \times [EtBr] \quad (vi)$$

where K_{app} is the apparent binding constant of the complex, $[Complex]_{50}$ is the concentration of the compound at which 50% of the DNA-EtBr has been quenched, K_{EtBr} is the binding constant of EtBr (K_{EtBr} = 1.0 × 10^7 M^{-1}), and [EtBr] is the concentration of ethidium bromide used in the EtBr displacement assay (8 μM).

5.6.3. Protein-Binding Studies. With the help of a tryptophan emission-quenching experiment, we detected the interaction of the complexes with protein BSA.[45,46] Initially, 2 × 10^{-6} M BSA solution was prepared in Tris-HCl/NaCl buffer. Then, aqueous solutions of the complexes were added to BSA solution with a regular increase in their concentrations. After each addition, the solutions were shaken slowly for 5 min, and the fluorescence at a wavelength of 295 nm (λ_{ex} = 295 nm) was recorded. A decrease in the fluorescence intensity of BSA at λ = 340 nm was observed upon increasing the concentration of

https://doi.org/10.1021/acsomega.3c01639
ACS Omega 2023, 8, 32382−32395

the complex due to the interaction between the complex and BSA. With the help of the Stern−Volmer eq vii, we quantitatively determine the quenching constant (K_{BSA}). We obtained a linear plot of I_0/I *vs* [complex] using eq vii with the help of Origin Lab, version 8.5.

$$\frac{I_0}{I} = 1 + K_{BSA}[Q] = 1 + k_q\tau_0[Q] \quad \text{(vii)}$$

where I_0 is the fluorescence intensity of BSA in the absence of the complex, I is the fluorescence intensity of BSA in the presence of a complex of concentration [Q], τ_0 is the lifetime of tryptophan in BSA (found as 1×10^{-8}), and k_q is the quenching constant. Equation viii gives the binding properties of the complexes.

$$\log\left(\frac{I_0 - I}{I}\right) = \log K + n \log[Q] \quad \text{(viii)}$$

where K is the binding constant and n is the number of binding sites.

5.6.4. Cytotoxicity Studies. The cells were cultured using DMEM (Himedia) media containing 10% FBS (Sigma-Aldrich), 1% nonessential amino acids (Himedia), and 1% antibiotic and antimitotic solution (Gibco). Cells were developed and incubated at 37 °C, with 95% relative humidity, in a CO_2 incubator in a T25 flask and monitored continuously using an inverted Olympus microscope. When 80% confluency was achieved, it was trypsinized and used for the MTT assay.[47] For the MTT assay, 24-well plates were reserved and seeded with 1×10^4 cells per well and incubated in a CO_2 incubator. After 24 h of incubation, the cells were treated with different drug concentrations of 6.25, 12.5, 25, 50, 100, and 150 μM. They were incubated for 24 h, and the cell viability was determined using MTT 3-(4,5-dimethylthiazol-2-yl)-2,5-diphenyltetrazolium bromide. Then, the resultant suspension was kept on a microvibrator for 10 min, and the absorbance was recorded at λ = 570 nm in an ELISA plate reader. The experiment was also performed in triplicate. Data were represented as the growth inhibition percentage, i.e., % growth inhibition = 100 − [(AD × 100)/AB], where AD is the measured absorbance in wells that contain samples and AB is the measured absorbance for blank wells (cells with the medium and the vehicle).

5.6.5. Cellular Localization Study. The colocalization of compound **7a** in U87MG cells was carried out using nucleus tracking dye DAPI and visualized for imaging studies *via* a confocal laser scanning microscope (CLSM 510, Zeiss, Oberkochen, Germany). U87MG cells were incubated with the IC_{50} value of complex **7a** for 4 h. After 4 h incubation, the cells were fixed with 4% formalin and lysed with 0.1 Triton X 100.

5.6.6. Scratch Wound Assay. An *in vitro* scratch wound assay was performed to determine the consequence of the synthesized complexes and untreated sample on migration. 24-well plates were taken, and 1×10^3 of HeLa cells were seeded in each well and cultured; they were sporadically scrutinized using an inverted microscope. When a monolayer of cells was formed, a sterile 100 μL tip was taken and scratched to create a gap in the 24-well plates. The culture media was removed and replaced with fresh media. 25 μM Complex was added to 24-well plates and monitored randomly at different time intervals of 0, 6, 12, 24, and 48 h to determine whether the gap created was either closed or inhibited by the complex.

5.6.7. ROS Generation by the DCFDA Staining Assay.[48] To verify the reactive oxygen species (ROS)-generating potential and following oxidative stress caused by complex **7a**, MCF-7 cells were stained with 2′,7′-dichlorofluorescein diacetate (DCFDA). The DCFDA oxidized by ROS exhibits a red fluorescence with excitation/emission at 485 nm/535 nm, respectively. Complex **7a** in a quantity equivalent to its IC_{50} value was added to MCF-7 cells and incubated at 37 °C, followed by the addition of 10 μM DCFH-DA and incubation for 2 h in a dark humidified atmosphere. The cells were again washed with 1 × PBS to remove excess dye and observed under an Olympus fluorescence microscope.

5.6.8. Cell Cycle Analysis.[48] Flow cytometry was performed to measure the DNA content in cells. This analysis is based on the ability to stain cellular DNA in a stoichiometric manner. Various dyes are available to serve this function, all of which have high binding affinities for DNA. The location where these dyes bind on the DNA molecule varies with the type of dye used. The DNA-binding dye used in this study was the most commonly used blue-excited dye propidium iodide. PI is an intercalating dye that binds to DNA and double-stranded RNA (and is thus almost always used in conjunction with RNaseA to remove RNA). When diploid cells stained with a dye that stoichiometrically binds to DNA are analyzed by flow cytometry, a "narrow" distribution of fluorescent intensities is obtained. 1×10^6 MCF-7 cells were seeded and cultured for 24 h in a 6-well plate containing 2 mL of media. Cells were then treated with desired concentrations of given samples prepared in media and incubated for another 24 h. Cells were then harvested and centrifuged at 2000 rpm for 5 min at room temperature, and the supernatant was discarded, carefully retaining the cell pellet. Next, the cell pellet was washed by suspending it in 2 mL of 1× PBS. The washing was repeated under the same conditions. The supernatant was discarded, retaining the pellet. Cells were fixed by suspending in 300 μL of sheath fluid, followed by adding 1 mL of chilled 70% EtOH drop by drop with continuous gentle shaking, and another 1 mL of chilled 70% EtOH was added at once. The cells were then stored at 4 °C overnight. After fixing, the cells were centrifuged at 2000 rpm for 5 min. The cell pellet was washed twice with 2 mL of cold 1× PBS. The cell pellet was then resuspended in 450 μL of sheath fluid containing 0.05 mg/ml PI and 0.05 mg/ml RNaseA and incubated for 15 min in the dark. The Beckmann Coulter flow cytometry was performed to determine the percentage of cells in various cell cycle stages in complex-treated and untreated populations. Data analysis was performed using FCS Express Version 5 software.

5.6.9. Apoptosis in MCF-7 Cells and the Annexin FITC/PI Assay. A day before the induction of apoptosis, 1×10^6 MCF-7 cells were seeded per well in a 6-well plate using a DMEM cell culture medium. After 24 h incubation, the media was replaced with a new culture medium to the original volume. The cells were treated with a potent complex to induce apoptosis with samples at two different concentrations and incubated for 24 h. Later, the collected cell culture medium was collected into Ria vials. Using a scrapper, the cells were detached from the dish, 1 mL of medium was added to each well, and the contents were transferred to identical Ria vials. The supernatant was separated by centrifugation and discarded. The cells were washed twice with cold PBS and then resuspended in 1 mL 1× binding buffer at a concentration of 1×10^6 cells/mL. 500 μL of cell suspension was aliquoted and 10 μL of propidium iodide and 5 μL of Annexin V were

https://doi.org/10.1021/acsomega.3c01639
ACS Omega 2023, 8, 32382−32395

added. The suspension was incubated for 15 min at room temperature under dark conditions. After incubation, the cells were analyzed by flow cytometry as soon as possible (within 1 h).

5.6.10. Statistical Analysis. As the study had more than one group, one-way ANOVA was used for statistical analysis. A *p*-value <0.05 was considered significant.

■ ASSOCIATED CONTENT

Supporting Information

The Supporting Information is available free of charge at https://pubs.acs.org/doi/10.1021/acsomega.3c01639.

Brief descriptions in nonsentence format listing the contents; ^{1}H, ^{31}P, and ^{19}F NMR, HRMS, FT-IR, UV, and fluorescence spectra of all compounds used in this study (PDF)

■ AUTHOR INFORMATION

Corresponding Author

Priyankar Paira − *Department of Chemistry, School of Advanced Sciences, Vellore Institute of Technology, Vellore 632014 Tamil Nadu, India;* orcid.org/0000-0003-1698-4895; Email: priyankar.paira@vit.ac.in

Author

Lavanya Thilak Babu − *Department of Chemistry, School of Advanced Sciences, Vellore Institute of Technology, Vellore 632014 Tamil Nadu, India*

Complete contact information is available at: https://pubs.acs.org/10.1021/acsomega.3c01639

Notes

The authors declare no competing financial interest.

■ ACKNOWLEDGMENTS

The authors are obliged to the Department of Science and Technology, Government of India, for supporting the work through the DST-SERB CRG project grant (CRG/2021/002267). The authors acknowledge ICMR (2019−6766 Nan-BMS) for the SRF to L.T.B. and the contingency grant. They acknowledge DST, New Delhi, India, for the DST-FIST project

■ LIST OF ABBREVIATIONS

NMR: nuclear magnetic resonance
ppm: parts per million
LLCT: ligand−ligand charge transfer
MLCT: metal−ligand charge transfer
MTT: 3-(4,5-dimethylthiazol-2-yl)-2,5-diphenyltetrazolium bromide
TLC: thin-layer chromatography
s: singlet
d: doublet
t: triplet
m: multiplet
OD: optical density
CT-DNA: calf thymus DNA

■ REFERENCES

(1) Jensen, H.; Nissen, A.; Vedsted, P. Quality Deviations in Cancer Diagnosis: Prevalence and Time to Diagnosis in General Practice. *Br. J. Gen. Pract.* **2014**, *64*, No. e92.

(2) Sung, H.; Ferlay, J.; Siegel, R. L.; Laversanne, M.; Soerjomataram, I.; Jemal, A.; Bray, F. Global Cancer Statistics 2020: GLOBOCAN Estimates of Incidence and Mortality Worldwide for 36 Cancers in 185 Countries. *CA: Cancer J. Clin.* **2021**, *71*, 209−249.

(3) Allardyce, C. S.; Dyson, P. J. Metal-Based Drugs That Break the Rules. *Dalton Trans.* **2016**, *45*, 3201−3209.

(4) Ndagi, U.; Mhlongo, N.; Soliman, M. E. Metal Complexes in Cancer Therapy − An Update from Drug Design Perspective. *Drug Des. Devel. Ther.* **2017**, *Volume11*, 599−616.

(5) Gibbs, J. B. Mechanism-Based Target Identification and Drug Discovery in Cancer Research. *Science* **2000**, *287*, 1969−1973.

(6) Ji, H.-F.; Li, X.-J.; Zhang, H.-Y. Natural Products and Drug Discovery. Can Thousands of Years of Ancient Medical Knowledge Lead Us to New and Powerful Drug Combinations in the Fight against Cancer and Dementia? *EMBO Rep.* **2009**, *10*, 194−200.

(7) Florea, A.-M.; Büsselberg, D. Cisplatin as an Anti-Tumor Drug: Cellular Mechanisms of Activity, Drug Resistance and Induced Side Effects. *Cancers* **2011**, *3*, 1351−1371.

(8) Sonkar, C.; Sarkar, S.; Mukhopadhyay, S. Ruthenium (II)−Arene Complexes as Anti- Metastatic Agents, and Related Techniques. *RSC Med. Chem.* **2022**, *13*, 22−38.

(9) Chakraborty, S.; Rahman, T. The Difficulties in Cancer Treatment. *Ecancermedicalscience* **2012**, *6*, No. ed16.

(10) Haas, K. L.; Franz, K. J. Application of Metal Coordination Chemistry to Explore and Manipulate Cell Biology. *Chem. Rev.* **2009**, *109*, 4921−4960.

(11) Zaki, M.; Hairat, S.; Aazam, E. S. Scope of Organometallic Compounds Based on Transition Metal-Arene Systems as Anticancer Agents: Starting from the Classical Paradigm to Targeting Multiple Strategies. *RSC Adv.* **2019**, *9*, 3239−3278.

(12) Kostova, I. Ruthenium Complexes as Anticancer Agents. *Curr. Med. Chem.* **2006**, *13*, 1085−1107.

(13) (a) Alessio, E. Thirty Years of the Drug Candidate NAMI-A and the Myths in the Field of Ruthenium Anticancer Compounds: A Personal Perspective. *Eur. J. Inorg. Chem.* **2017**, *2017*, 1549−1560. (b) Jiang, G.-B.; Zhang, W.-Y.; He, M.; Gu, Y.-Y.; Bai, L.; Wang, Y.-J.; Yi, Q.-Y.; Du, F. New Ruthenium Polypyridyl Complexes Functionalized with Fluorine Atom or Furan: Synthesis, DNA-Binding, Cytotoxicity and Antitumor Mechanism Studies. *Spectrochim. Acta, Part A* **2020**, *227*, No. 117534. (c) Jiang, G.-B.; Zhang, W.-Y.; He, M.; Gu, Y.-Y.; Bai, L.; Wang, Y.-J.; Yi, Q.-Y.; Du, F. Development of Four Ruthenium Polypyridyl Complexes as Antitumor Agents: Design, Biological Evaluation and Mechanism Investigation. *J. Inorg. Biochem.* **2020**, *208*, No. 111104.

(14) Artner, C.; Holtkamp, H. U.; Hartinger, C. G.; Meier-Menches, S. M. Characterizing Activation Mechanisms and Binding Preferences of Ruthenium Metallo-Prodrugs by a Competitive Binding Assay. *J. Inorg. Biochem.* **2017**, *177*, 322−327.

(15) (a) Kenny, R. G.; Marmion, C. J. Toward Multi-Targeted Platinum and Ruthenium Drugs-A New Paradigm in Cancer Drug Treatment Regimens? *Chem. Rev.* **2019**, *119*, 1058−1137. (b) Trondl, R.; Heffeter, P.; Kowol, C. R.; Jakupec, M. A.; Berger, W.; Keppler, B. K. NKP-1339, the First Ruthenium-Based Anticancer Drug on the Edge to Clinical Application. *Chem. Sci.* **2014**, *5*, 2925−2932. (c) Ang, W. H.; Casini, A.; Sava, G.; Dyson, P. J. Organometallic Ruthenium-Based Antitumor Compounds with Novel Modes of Action. *J. Organomet. Chem.* **2011**, *696*, 989−998.

(16) Zeng, L.; Gupta, P.; Chen, Y.; Wang, E.; Ji, L.; Chao, H.; Chen, Z.-S. The Development of Anticancer Ruthenium(II) Complexes: From Single Molecule Compounds to Nanomaterials. *Chem. Soc. Rev.* **2017**, *46*, 5771−5804.

(17) Smithen, D. A.; Yin, H.; Beh, M. H. R.; Hetu, M.; Cameron, T. S.; McFarland, S. A.; Thompson, A. Synthesis and Photobiological Activity of Ru(II) Dyads Derived from Pyrrole-2-Carboxylate Thionoesters. *Inorg. Chem.* **2017**, *56*, 4121−4132.

(18) Rademaker-Lakhai, J. M.; van den Bongard, D.; Pluim, D.; Beijnen, J. H.; Schellens, J. H. M. A Phase I and Pharmacological Study with Imidazolium-Trans-DMSOImidazole- Tetrachlororuthen-

ate, a Novel Ruthenium Anticancer Agent. *Clin. Cancer Res.* **2004**, *10*, 3717−3727.
(19) Monro, S.; Colón, K. L.; Yin, H.; Roque, J. I. I. I.; Konda, P.; Gujar, S.; Thummel, R. P.; Lilge, L.; Cameron, C. G.; McFarland, S. A. Transition Metal Complexes and Photodynamic Therapy from a Tumor-Centered Approach: Challenges, Opportunities, and Highlights from the Development of TLD1433. *Chem. Rev.* **2019**, *119*, 797−828.
(20) McFarland, S. A.; Mandel, A.; Dumoulin-White, R.; Gasser, G. Metal-Based Photosensitizers for Photodynamic Therapy: The Future of Multimodal Oncology? *Curr. Opin. Chem. Biol.* **2020**, *56*, 23−27.
(21) Ma, D.-L.; Wu, C.; Wu, K.-J.; Leung, C.-H. Iridium(III) Complexes Targeting Apoptotic Cell Death in Cancer Cells. *Molecules* **2019**, *24*, 2739.
(22) Hearn, J. M.; Romero-Canelón, I.; Qamar, B.; Liu, Z.; Hands-Portman, I.; Sadler, P. J. Organometallic Iridium(III) Anticancer Complexes with New Mechanisms of Action: NCI-60 Screening, Mitochondrial Targeting, and Apoptosis. *ACS Chem. Biol.* **2013**, *8*, 1335−1343.
(23) Sun, Q.; Wang, Y.; Fu, Q.; Ouyang, A.; Liu, S.; Wang, Z.; Su, Z.; Song, J.; Zhang, Q.; Zhang, P.; Lu, D. Sulfur-Coordinated Organoiridium(III) Complexes Exert Breast Anticancer Activity via Inhibition of Wnt/β-Catenin Signaling. *Angew. Chem. Int. Ed.* **2021**, *60*, 4841−4848.
(24) Wang, W.-J.; Ling, Y.-Y.; Zhong, Y.-M.; Li, Z.-Y.; Tan, C.-P.; Mao, Z.-W. Ferroptosis-Enhanced Cancer Immunity by a Ferrocene-Appended Iridium(III) Diphosphine Complex. *Angew. Chem., Int. Ed.* **2022**, *61*, No. e202115247.
(25) Konkankit, C. C.; King, A. P.; Knopf, K. M.; Southard, T. L.; Wilson, J. J. In Vivo Anticancer Activity of a Rhenium(I) Tricarbonyl Complex. *ACS Med. Chem. Lett.* **2019**, *10*, 822−827.
(26) Pan, Z.-Y.; Cai, D.-H.; He, L. Dinuclear Phosphorescent Rhenium(i) Complexes asPotential Anticancer and Photodynamic Therapy Agents. *Dalton Trans.* **2020**, *49*, 11583−11590.
(27) Subasinghe, A.; Perera, I. C.; Pakhomova, S.; Perera, T. Synthesis, Characterization,and Biological Studies of a Piperidinyl Appended Dipicolylamine Ligand and Its Rhenium Tricarbonyl Complex as Potential Therapeutic Agents for Human Breast Cancer. *Bioinorg. Chem. Appl.* **2016**, *2016*, No. 2675937.
(28) Irfan, A.; Batool, F.; Zahra Naqvi, S. A.; Islam, A.; Osman, S. M.; Nocentini, A.; Alissa, S. A.; Supuran, C. T. Benzothiazole Derivatives as Anticancer Agents. *J. Enzyme Inhib. Med. Chem.* **2020**, *35*, 265−279.
(29) Kubanik, M.; Holtkamp, H.; Söhnel, T.; Jamieson, S. M. F.; Hartinger, C. G. Impact of the Halogen Substitution Pattern on the Biological Activity of Organoruthenium 8- Hydroxyquinoline Anticancer Agents. *Organometallics* **2015**, *34*, 5658−5668.
(30) Munteanu, A.-C.; Badea, M.; Olar, R.; Silvestro, L.; Dulea, C.; Negut, C.-D.; Uivarosi, V. Synthesis and Structural Investigation of New Bio-Relevant Complexes of Lanthanides with 5- Hydroxyflavone: DNA Binding and Protein Interaction Studies. *Molecules* **2016**, *21*, 1737.
(31) Lohani, N.; Singh, H. N.; Moganty, R. R. Structural Aspects of the Interaction of Anticancer Drug Actinomycin-D to the GC Rich Region of Hmgb1 Gene. *Int. J. Biol. Macromol.* **2016**, *87*, 433−442.
(32) Rajesh, J.; Rajasekaran, M.; Rajagopal, G.; Athappan, P. Analytical Methods to Determine the Comparative DNA Binding Studies of Curcumin-Cu(II) Complexes. *Spectrochim. Acta, Part A* **2012**, *97*, 223−230.
(33) Chandra, A.; Singh, K.; Singh, S.; Sivakumar, S.; Patra, A. K. A Luminescent Europium(III)− Platinum(II) Heterometallic Complex as a Theranostic Agent: A Proof-of-Concept Study. *Dalton Trans.* **2016**, *45*, 494−497.
(34) Wang, Y.-Q.; Hongmei, Z.; Gencheng, Z.; Weihua, T.; Shuhe, T. Interaction of the Flavonoid Hesperidin with Bovine Serum Albumin: A Fluorescence Quenching Study. *J. Lumin.* **2007**, *126*, 211−218.
(35) Yasmeen, S.; Riyazuddeen. Exploring Thermodynamic Parameters and the Binding Energetic of Berberine Chloride to Bovine Serum Albumin (BSA): Spectroscopy, Isothermal Titration Calorimetry and Molecular Docking Techniques. *Thermochim. Acta* **2017**, *655*, 76−86.
(36) Gharagozlou, M.; Boghaei, D. M. Interaction of Water-Soluble Amino Acid Schiff Base Complexes with Bovine Serum Albumin: Fluorescence and Circular Dichroism Studies. *Spectrochim. Acta, Part A* **2008**, *71*, 1617−1622.
(37) Jonkman, J. E. N.; Cathcart, J. A.; Xu, F.; Bartolini, M. E.; Amon, J. E.; Stevens, K. M.; Colarusso, P. An Introduction to the Wound Healing Assay Using Live-Cell Microscopy. *Cell Adhes. Migr.* **2014**, *8*, 440−451.
(38) Darzynkiewicz, Z.; Juan, G.; Li, X.; Gorczyca, W.; Murakami, T.; Traganos, F. Cytometry in Cell Necrobiology: Analysis of Apoptosis and Accidental Cell Death (Necrosis). *Cytometry* **1997**, *27*, 1−20.
(39) Nakanishi, M.; Shimada, M.; Niida, H. Genetic Instability in Cancer Cells by Impaired Cell Cycle Checkpoints. *Cancer Sci.* **2006**, *97*, 984−989.
(40) Cury-Boaventura, M. F.; Pompéia, C.; Curi, R. Comparative Toxicity of Oleic Acid and Linoleic Acid on Jurkat Cells. *Clin. Nutr.* **2004**, *23*, 721−732.
(41) Baskić, D.; Popović, S.; Ristić, P.; Arsenijević, N. N. Analysis of Cycloheximide- Induced Apoptosis in Human Leukocytes: Fluorescence Microscopy Using Annexin V/Propidium Iodide versus Acridin Orange/Ethidium Bromide. *Cell Biol. Int.* **2006**, *30*, 924−932.
(42) Shamsi-Sani, M.; Shirini, F.; Abedini, M.; Seddighi, M. Synthesis of Benzimidazole and Quinoxaline Derivatives Using Reusable Sulfonated Rice Husk Ash (RHA-SO_3H) as a Green and Efficient Solid Acid Catalyst. *Res. Chem. Intermed.* **2016**, *42*, 1091−1099.
(43) Nikolić, S.; Rangasamy, L.; Gligorijević, N.; Aranđelović, S.; Radulović, S.; Gasser, G.; Grgurić-Šipka, S. Synthesis, Characterization and Biological Evaluation of Novel Ru(II)-Arene Complexes Containing Intercalating Ligands. *J. Inorg. Biochem.* **2016**, *160*, 156−165.
(44) Dasari, S.; Patra, A. K. Luminescent Europium and Terbium Complexes of Dipyridoquinoxaline and Dipyridophenazine Ligands as Photosensitizing Antennae: Structures and Biological Perspectives. *Dalton Trans.* **2015**, *44*, 19844−19855.
(45) Keizer, J. Nonlinear Fluorescence Quenching and the Origin of Positive Curvature in Stern-Volmer Plots. *J. Am. Chem. Soc.* **1983**, *105*, 1494−1498.
(46) Suryawanshi, V. D.; Walekar, L. S.; Gore, A. H.; Anbhule, P. V.; Kolekar, G. B. Spectroscopic Analysis on the Binding Interaction of Biologically Active Pyrimidine Derivative with Bovine Serum Albumin. *J. Pharm. Anal.* **2016**, *6*, 56−63.
(47) Liu, P.; Wu, B.-Y.; Liu, J.; Dai, Y.-C.; Wang, Y.-J.; Wang, K.-Z. DNA Binding and Photocleavage Properties, Cellular Uptake and Localization, and in-Vitro Cytotoxicity of Dinuclear Ruthenium(II) Complexes with Varying Lengths in Bridging Alkyl Linkers. *Inorg. Chem.* **2016**, *55*, 1412−1422.
(48) Mondal, A.; Shanavas, S.; Sen, U.; Das, U.; Roy, N.; Bose, B.; Paira, P. Mitochondria-Targeted Half-Sandwich Iridium(III)-Cp*-Arylimidazophenanthroline Complexes as Antiproliferative and Bioimaging Agents against Triple Negative Breast Cancer Cells MDA-MB-468. *RSC Adv.* **2022**, *12*, 11953−11966.

https://doi.org/10.1021/acsomega.3c01639
ACS Omega 2023, 8, 32382−32395